Chinese Journal of Physics 93 (2025) 564–576

Contents lists available at ScienceDirect

Chinese Journal of Physics

journal homepage: www.sciencedirect.com/journal/chinese-journal-of-physics

Research Paper

First-principles study on the structural, mechanical and optoelectronic properties of the hydrogenated and fluorinated dumbbell silicene monolayers and their vertical heterostructures

Gang Guo [a,*], Fuming Du [b], Gencai Guo [c], Ping Li [d,*]

[a] School of Science, Hunan Institute of Technology, Hengyang 421002, China
[b] School of Materials Science and Engineering, Hunan Institute of Technology, Hengyang 421002, China
[c] Hunan Key Laboratory for Micro-Nano Energy Materials and Devices and School of Physics and Optoelectronics, Xiangtan University, Hunan, 411105, China
[d] State Key Laboratory for Mechanical Behavior of Materials, Center for Spintronics and Quantum System, School of Materials Science and Engineering, Xi'an Jiaotong University, Xi'an 710049, China

ARTICLE INFO

Keywords:
Dumbbell silicene monolayers
Vertical heterostructures
Type-II band alignment
Optoelectronic properties
Chemical functionalization

ABSTRACT

Using first-principles calculations, we systematically investigate the structural, mechanical, and optoelectronic properties of hydrogenated and fluorinated dumbbell silicene (DB-SiH and DB-SiF) monolayers, as well as their vertical heterostructures. Ab initio molecular dynamics (AIMD) calculations demonstrate that both the DB-SiH and DB-SiF monolayers, along with their heterostructures, exhibit excellent structural and thermal stability. Furthermore, hydrogenation and fluorination can increase the band gap of dumbbell silicene, resulting in a direct band gap of 1.99 eV and an indirect band gap of 1.55 eV, respectively. The work function of dumbbell silicene can be effectively tuned by the chemical functionalization. The DB-SiH/DB-SiF heterostructures display direct band gap characteristics and a typical type-II band alignment. Notably, the significant charge transfer from DB-SiH to DB-SiF induces a built-in electric field at the interface of the heterostructures, which facilitates the separation of electrons and holes. Additionally, the DB-SiH/DB-SiF heterostructures exhibit enhanced visible light absorption coefficients compared to those of the individual monolayers. The interesting findings suggest that these novel structures hold valuable potential for applications in optoelectronics.

1. Introduction

Since the successful synthesis of two-dimensional (2D) planar graphene [1], it has continuously become a research hotspot due to its excellent optical, and electrical properties [2,3]. Coincidentally, a graphene-like 2D material, low-buckled silicene (LB-silicene) [4] has received much attention. Compared with the planar graphene with the sp^2 hybridization [5], the LB-silicene has a sp^2/sp^3-bonded hexagonal lattice [6]. Researchers have discovered many novel properties of LB-silicene such as high carrier mobility [7], giant magnetoresistance [8], outstanding mechanical flexibility [9,10], and strong spin-orbit coupling [11], which shows its potential applications in electronic equipment and nanotechnology. Furthermore, in the experiment, LB-silicene has been successfully synthesized by growing it on Ag (111) [12], Au (111) [13], and Al (111) [14] substrates. The useful experimental results have effectively

* Corresponding authors.
E-mail addresses: ggxhsg@126.com (G. Guo), pli@xjtu.edu.cn (P. Li).

https://doi.org/10.1016/j.cjph.2024.12.029
Received 15 October 2024; Received in revised form 5 December 2024; Accepted 30 December 2024
Available online 31 December 2024

validated the theoretical predictions of LB-silicene, which also encourages researchers to explore other allotropes.

Fortunately, previous studies [15,16] reported that the silicon (Si) atoms adsorbed on the surface of LB-silicene can lead to a new silicon allotrope with a dumbbell (DB) structure. Unlike the semi-metallic nature of LB-silicene, the DB-silicene exhibits a semiconducting character with an indirect band gap of 0.73 eV [17], suggesting its advantages in the application of photoelectric devices. Although the experimental synthesis of DB-silicene has not been achieved yet, theoretical research [18] suggests that DB-silicene is more energetically favorable due to its lower total energy per atom compared to LB-silicene [18], indicating the potential for experimental preparation. To date, various intrinsic physical properties of pristine DB-silicene, including electronic, optical, magnetic, thermal conductivity, phonon transport, and thermal transport properties, have been systematically investigated [18–21]. However, research on the modification of DB-silicene remains limited. To further enhance the properties of DB-silicene and explore its potential applications in optoelectronic devices, it is essential to improve its optoelectronic characteristics through targeted control methods.

Many effective methods such as applying strain and electric field [22,23], atomic and molecular doping [24,25], surface functionalization [26,27], and constructing heterojunction [28–30] have been proposed to regulate the physical properties of nano-materials. In particular, due to the high specific surface area of 2D nanomaterials, surface chemical functionalization becomes a new way to modify the intrinsic physical properties. For example, a first-principles study [31] reported that the electronic and optical properties of 2D Pentagermanene monolayer can be effectively tuned by hydrogen or fluorine functionalization. Another ab initio calculation [32] demonstrated that nitrogen functionalisation can transform the MgO monolayer from a semiconductor to a metal, whereas fluorine functionalization can result in a substantial narrowing of the band gap. Moreover, after functionalization, the optical absorption in the infrared and visible regions of the MgO monolayer can be markedly enhanced. Hoat et al. [33] have demonstrated that halogen atoms functionalization can result in a notable expansion of the band gap of LB-germanene, thus providing a valuable reference point for the potential applications of germanene in optoelectronic devices. As for LB-silicene, surface functionalization allows for convenient control of its photoelectric properties. For instance, Bao et al. [34] demonstrated that the electronic and optical properties of LB-silicene can be significantly enhanced through halogen atom functionalization. The findings of their study demonstrated that the direct band gap can be reduced from 1.53 to 2.12 eV through full- and Janus-functionalization, thereby enhancing the optical absorption of the material in both the visible and ultraviolet regions. Our group conducted a comprehensive investigation into the effects of Janus-functionalization on LB-silicene, employing the functionalization of H and alkali metal atoms or halogen atoms [35,36]. It was demonstrated that the H and Li Janus-functionalization can confer a metallic nature and magnetic behaviour upon LB-silicene. Furthermore, the H and X (X=F, Cl and Br) Janus-functionalization was shown to induce notable photocatalytic performance for water splitting of LB-silicene, thereby broadening the potential applications of LB-silicene in the field of optoelectronics.

Up to now, the impact of surface chemical functionalization on the structural stability, mechanical and optoelectronic properties of DB-silicene monolayer has not been subjected to a comprehensive and systematic investigation. It remains unclear whether the indirect band gap of the DB-silicene monolayer can be transformed into a direct band gap through chemical functionalization. It would be beneficial to ascertain whether chemical functionalization affects the optical absorption of the DB-silicene monolayer? What are the effects of interfacial interactions on the physical properties of surface-functionalised bilayer DB-silicene? In order to address the aforementioned issues, this paper employs first-principles calculations to systematically investigate the structural, mechanical, and optoelectronic properties of hydrogenated and fluorinated DB-silicene (DB-SiH and DB-SiF) monolayers. Furthermore, the optoelectronic properties of the heterostructures formed by DB-SiH and DB-SiF monolayers are also investigated in detail. The results demonstrate that the hydrogenated and fluorinated DB-silicene monolayers as well as their heterostructures exhibit remarkable structural stability, excellent mechanical properties, and improved optoelectronic properties. Notably, hydrogenation can impart a direct bandgap of 1.55 eV to DB-silicene, while fluorination can markedly enhance this to approximately 2.00 eV. All the heterostructures exhibit direct band gaps with type-II band alignment and enhanced optical absorption in the visible and ultraviolet regions. In light of the successful preparation of halogenated graphene [37] and hydrogenated LB-silicene monolayer [38], it is plausible that the functionalised DB-silicene monolayers presented in this work could be prepared experimentally in the future.

2. Computational methods

In this work, all calculations were performed with the help of the Vienna ab initio simulation package (VASP) based on density functional theory (DFT) [39,40]. The exchange-correlation functional was described using the Perdew-Burke-Ernzerhof (PBE) within Generalized Gradient Approximation (GGA) [41,42]. The convergence criteria for energy, the cut-off energy and force on each atom were set at 10^{-5} eV, 600 eV and 10^{-2} eV/Å, respectively. A 15 × 15 × 1 k-mesh was used for the calculations of structure optimization and mechanical property, while a 21 × 21 × 1 k-mesh was selected for the calculations of optoelectronic properties. The vacuum spacing larger than 18 Å was used to mitigate the interlayer interactions between adjacent cells. For the accuracy of band structure calculation, the Heyd-Scuseria-Ernzerhof hybrid functional (HSE06) [43,44] was also used in electronic structure calculations. Additionally, the van der Waals (vdW) interaction in DB-SiH/DB-SiF heterostructures was considered in calculations. To check the thermal stability of studied systems at room temperature, we performed the ab initio molecular dynamics (AIMD) simulations at room temperature using a 2 × 2 × 1 supercell. Meanwhile, we also calculated cohesive energy per atom (E_c) and binding energy (E_b) to examine the energetic stability of the monolayers and heterostructures, respectively, which can be expressed as follows [45,46]:

$$E_c = \left(E_t - \sum n_x E_x\right) \Big/ N \tag{1}$$

$$E_b = E_{DB-SiH/DB-SiF} - E_{DB-SiH} - E_{DB-SiF} \tag{2}$$

where E_t and E_x represent the total energy of the system and the total energy of single atom (Si, H and F atoms). N is the the overall number of atoms in the cell, while n is the number of isolated atom x. The $E_{DB\text{-}SiH/DB\text{-}SiF}$, $E_{DB\text{-}SiH}$ and $E_{DB\text{-}SiF}$ are the total energy of DB-SiH/DB-SiF heterostructure, DB-SiH and DB-SiF monolayer, respectively. Here, a negative feature of E_c and E_b means the structural stability of the corresponding system.

The work function (W) is calculated by following equation [47]:

$$W = E_V - E_F \tag{3}$$

where the vacuum energy and the Fermi energy are represented by E_V and E_F, respectively.

To study the charge transfer of the system, the charge density difference (ΔQ) is also calculated. In monolayer and heterostructure systems, the ΔQ is calculated by following equations:

$$\Delta Q = Q_{tot} - Q_{DB-Si} - Q_x \tag{4}$$

$$\Delta Q = Q_{tot} - Q_{DB-SiH} - Q_{DB-SiF} \tag{5}$$

where Q_{tot}, $Q_{DB\text{-}Si}$, Q_x, $Q_{DB\text{-}SiH}$ and $Q_{DB\text{-}SiF}$ represent the the Mulliken charges of the whole system, pristine DB-silicene monolayer, x (H and F) atom, hydrogenated and fluorinated DB-silicene monolayers, respectively.

3. Results and discussions

3.1. Pristine DB-silicene monolayer

For comparison, the structural, and electronic properties of pristine DB-silicene are are initially examined. Fig. 1(a) depicts the optimized structure of pristine DB-silicene within a $2 \times 2 \times 1$ supercell. It can be observed that the unit cell comprises ten Si atoms. The lattice constant (a = b) and the buckled height between the upper and lower silicon atoms are 7.428 Å and 2.71 Å, respectively. As illustrated in Fig. 1(b-c), a notable charge overlap is evident between these Si-Si bonds. Concomitantly, the electron localization

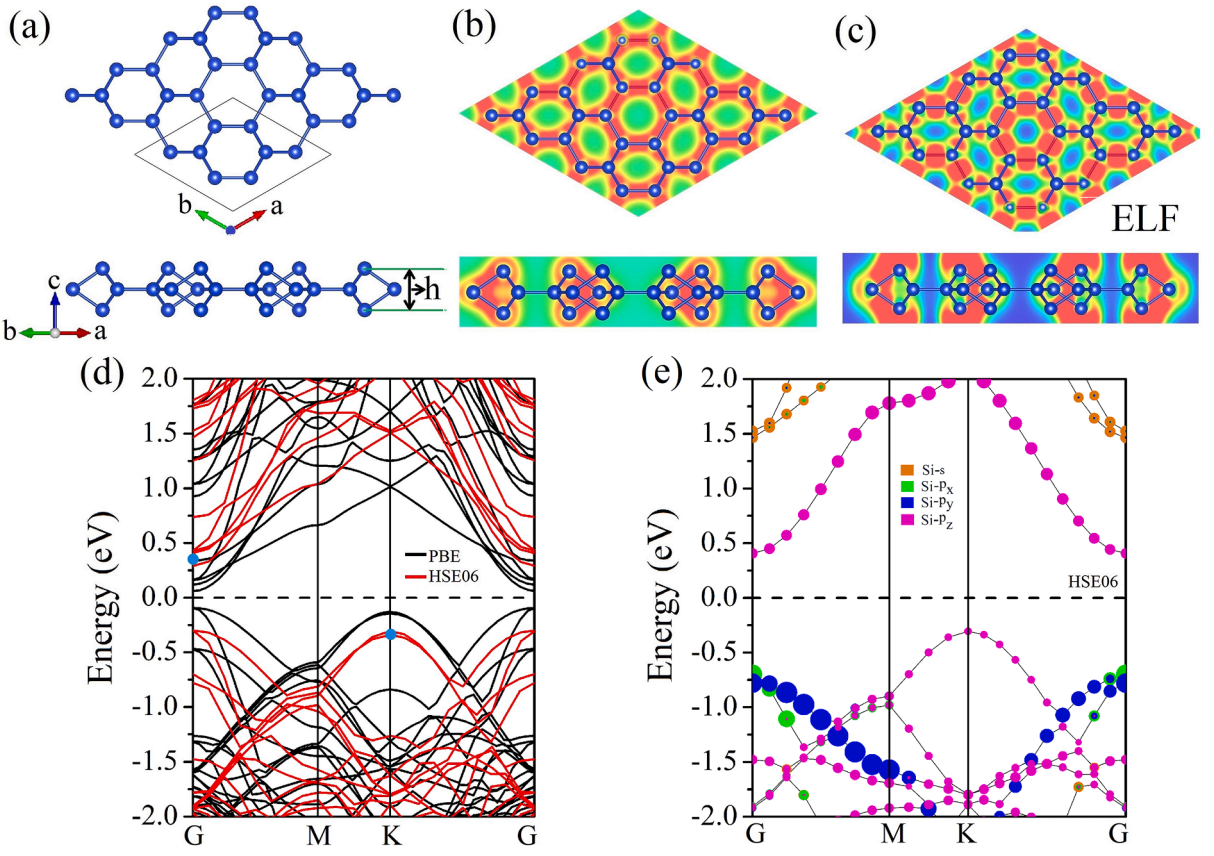

Fig. 1. (a) Top view and side view of the dumbbell silicene (DB-Si) monolayer. (b) The distributions of charge density. (c) Electron localization function (ELF). (d) The band structures calculated by PBE and HSE06 methods. (e) The orbital-resolved band structure. The Fermi level is at 0 eV.

function (ELF) value between silicon atoms is as high as 0.9. Furthermore, the charge densities are distributed among the silicon atoms, which indicates the presence of a clear covalent bond between the Si-Si bonds. Fig. 1(d) shows the band structures of the pristine DB-silicene monolayer, as calculated using the PBE and HSE06 methods. The top of the valence band is situated at the K-point within the Brillouin zone, while the bottom of the conduction band is located at the G-point within the Brillouin zone, indicating an indirect band gap of 0.72 eV (HSE06). Concurrently, the band structure curve calculated by the PBE method exhibits a similar trend to that of the HSE06 method, yet displays a lower band gap of 0.25 eV. The aforementioned structural and electronic properties are well in accordance with previously reported values [16], thereby demonstrating the accuracy of our calculation. In order to gain further insight into the role of atomic orbitals of Si in the electronic structure, the orbital-resolved band structure of DB-silicene monolayer is discussed in Fig. 1(e). It can be observed that the valence band maximum (VBM) and conduction band minimum (CBM) are predominantly derived from the Si-p_z orbital. Previous studies [17,21] have also demonstrated the structural stability of the pristine DB-silicene monolayer through phonon spectrum and AIMD analysis. The structural stability of the DB-silicene is also evaluated through the calculation of the cohesive energy (Table 1), which yielded a favourable value of -5.28 eV, thus further verifying its stability.

3.2. DB-SiH and DB-SiF monolayers

Fig. 2 gives the relaxed structures, the ELF and corresponding distributions of charge density difference (CDD) of DB-SiH and DB-SiF monolayers. As shown in Fig. 2 (a)-(b) and Table 1, the lattice constant, the Si-H (F) bond distance, and the buckled height between the upper and lower silicon atoms in the DB-SiH and DB-SiF cases are 7.382 Å (7.432 Å), 1.50 Å (1.62 Å) and 2.83 Å (2.72 Å), respectively. It is evident that upon fluorination, the crystal structure of DB-silicene undergoes less alteration compared to hydrogenation. The calculated cohesive energy of DB-SiF is -6.32 eV, which is more negative than the -4.72 eV observed in DB-SiH, indicating that DB-SiF is more stable. A similar trend has been reported for fluorinated LB-germanene [33]. The chemical bonds of DB-SiH and DB-SiF monolayers are examined through analysis of the ELF and corresponding CDD. As shown in Fig. 2 (c)-(d), the ELF value between silicon atoms is approximately 0.9, with charge density distributed among the silicon atoms, suggesting significant covalent bonding of the Si-Si bond. However, the substantial charge density between Si and H (F) atoms demonstrates a pronounced directionality towards H and F atoms, indicating predominant ionic bond characteristics in the Si-H and Si-F bonds. This is further supported by the CDD analysis. Specifically, in a Si-F bond, each F atom can acquire 0.80 e from the connected Si atom, exceeding the 0.53 e in the Si-H bond, attributed to the higher electronegativity of F (4.0) compared to H (2.1). Subsequently, AIMD simulations at room temperature are conducted to enhance the understanding of the stability of hydrogenated and fluorinated DB-silicene monolayers. As depicted in Fig. 3 (a)-(b), the total energy per atom in the DB-SiH case fluctuates between -4.53 and -4.56 eV, while in the case of DB-SiF, it fluctuates between -5.11 and -5.15 eV. Moreover, the final structures post-heating maintain a reasonable configuration without deformation, indicating their structural stability.

The mechanical properties of DB-SiH and DB-SiF monolayers are also studied. Via calculating linear elastic constants with the energy-strain method [48], the Young's Modulus (Y), Poisson's Ratio (V) and Shear Modulus (G) can be obtained from following equations:

$$Y = \left(C_{11}^2 - C_{12}^2\right)/C_{11} \tag{6}$$

$$V = C_{12}/C_{11} \tag{7}$$

$$G = (C_{11} - C_{12})/2 \tag{8}$$

According to our calculations listed in Table 3, the calculated elastic constants meet the following relations: $C_{11} = C_{22}$, $C_{66} = (C_{11}-C_{12})/2 > 0$, $C_{11} > 0$, $C_{11} > |C_{12}|$ and $C_{11}C_{22}$-$C_{12}^2 > 0$. These equations satisfy the criterion of mechanical stability of hexagonal 2D monolayers [49], indicating that the pristine DB-silicene, DB-SiH and DB-SiF monolayers are mechanically stable. In the case of pristine DB-silicene, the values of Y and G are 70.62 N/m and 26.70 N/m, respectively. For the DB-SiH and DB-SiF monolayers, the Y and G values are 72.18 N/m and 28.00 N/m, and 72.20 N/m and 27.26 N/m, respectively. It is observed that the Y and G values of the DB-SiH and DB-SiF monolayers exceed those of pristine DB-silicene, indicating superior rigidity and shear deformation resistance. Additionally, the V values for pristine DB-silicene, DB-SiH, and DB-SiF monolayers are 0.31, 0.29, and 0.32, respectively. These values are also higher than those of other 2D monolayers such as fluorinated LB-Silicene (~0.15) [34], graphene (~0.18) [49], and MoS_2 (~0.25) [50], demonstrating good mechanical properties of the studied structures.

The band structures of the DB-SiH and DB-SiF monolayers are calculated using the PBE and HSE06 methods. As illustrated in Fig. 4

Table 1
Some calculated parameters: the lattice parameters (a and b), bond length (d), the buckled height (h), cohesive energy (E_c), bandgaps (E_g) calculated by PBE and HSE06 methods, the work function (W) and the amount of charge transfer from Si to H or F atom.

Systems	a=b (Å)	d_{Si-H} (Å)	d_{Si-F} (Å)	h (Å)	E_c (eV)	E_g^{PBE} (eV)	E_g^{HSE06} (eV)	W (eV)	C (e)
DB-Si	7.428	/	/	2.71	-5.28	0.25	0.72 (I)	4.78	/
DB-SiH	7.382	1.50	/	2.83	-4.72	1.33	1.99 (D)	4.32	0.53
DB-SiF	7.432	/	1.62	2.72	-6.32	0.90	1.55 (I)	5.20	0.80

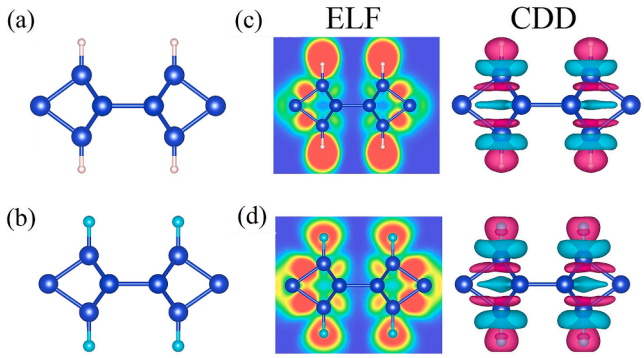

Fig. 2. The relaxed strictures, the electron localization function (ELF) and corresponding distributions of charge density difference of (a) DB-SiH and (b) DB-SiF. The value of the isosurface of CDD is 0.004 e/Å^3.

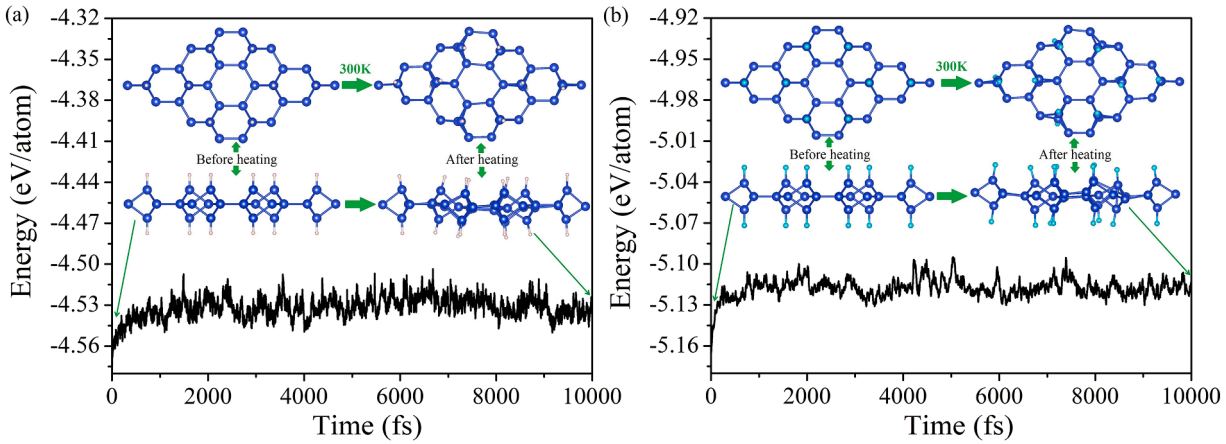

Fig. 3. The results of AIMD for (a) DB-SiH and (b) DB-SiF monolayers. Here the supercell lattices denote the initial and final structures before and after heating.

(a), hydrogenation results in the formation of a direct band gap in the DB-Silicene monolayer. The CBM and VBM are both situated at the G point of the Brillouin zone, resulting in a direct band gap of 1.99 eV. Conversely, fluorination, as illustrated in Fig. 4(b), results in an indirect band gap of 1.55 eV, with the CBM situated at the G point and the VBM at the K point of the Brillouin zone. This differs from the direct gap observed in the LB-Silicene monolayer with fluorination, as reported in reference [51]. A previous study [31] has reported that hydrogenated and fluorinated decorations in 2D Pentagermanene can give rise to distinct influences on the characteristics of the CBM and VBM states. To gain further insights into the electronic structure, the partial density of states (PDOS) and the distributions of the CBM and VBM of the DB-SiH and DB-SiF monolayers are discussed in the following sections. Fig. 5(a) illustrates that in the DB-SiH case, the VBM is predominantly contributed by the p orbital of the Si atom, while the CBM originates mainly from the s and

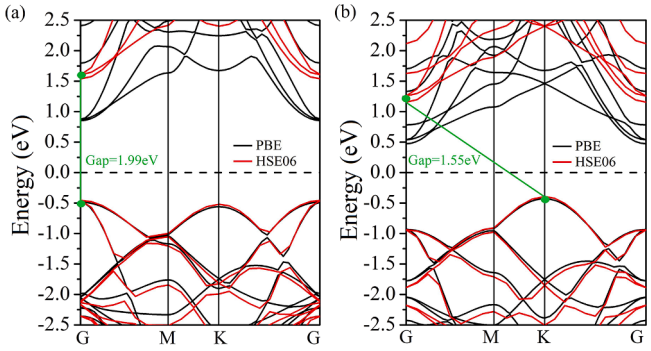

Fig. 4. (a) The band structures of (a) DB-SiH and (b) DB-SiF calculated by PBE and HSE06 methods. The Fermi level is at 0 eV.

p orbitals of the Si atom. Additionally, the H atoms contribute to the electronic state of the CBM to a limited extent. In contrast, the DB-SiF monolayer, as illustrated in Fig. 5(b), exhibits comparable contributions to the CBM and VBM from the Si atom to those observed in DB-SiH. However, the F atom does contribute to the electronic states of CBM and VBM. It is noteworthy that the band gap of the DB-SiF monolayer is lower than that of the DB-SiH monolayer, which is consistent with the findings of previous band structure analyses. This difference is attributed to the higher electronegativity of the fluorine atom compared to that of the hydrogen atom, resulting in a stronger Si-F bond than the H-Si bond. This alteration in the electronic structure leads to a smaller band gap.

The work functions of the pristine DB-silicene, DB-SiH, and DB-SiF monolayers are presented in Fig. 6. As shown in Fig. 6(a), the work function of the pristine DB-silicene monolayer is observed to be 4.78 eV. In contrast, the work functions of the DB-SiH and DB-SiF monolayers are 4.32 eV and 5.20 eV, respectively (Fig. 6b and c). A notable discrepancy in work function is apparent between the pristine DB-silicene monolayer and its hydrogenated and fluorinated counterparts. This variation can be attributed to the differing bond strengths between the silicon atoms and the hydrogen or fluorine atoms, which consequently influence the electronic structure of DB-silicene and result in alterations in the work function. In particular, the higher electronegativity of fluorine atoms enables them to extract electrons from the DB-silicene surface, thereby reducing the surface electron concentration and elevating the work function.

3.3. The DB-SiH/DB-SiF heterostructures

Given the analogous lattice constants of DB-SiH and DB-SiF monolayers, a vertical heterostructure formed by them exhibits a mere 0.67 % lattice mismatch. The present study investigates three distinct stacking configurations of DB-SiH/DB-SiF heterostructures, namely patterns AA, AB, and AC, respectively, as illustrated in Fig. 7. The relaxed lattice constant, Si-H and Si-F bond lengths for all heterostructures are 7.404 Å, 1.50 Å, and 1.62 Å, respectively, as listed in Table 2. The interlayer distances are 8.57 Å (AA), 8.54 Å (AB), and 8.56 Å (AC), respectively. The binding energies of the heterostructures are found to be negative, indicating their good stability. Particularly, the absolute value of binding energy per cell for the AB heterostructure is 132 meV, which is slightly higher than that of the AA heterostructure and significantly higher than that of the AC heterostructure. Therefore, the AB heterostructure is the most stable. In light of the similarities in properties between the AB and AC heterostructures, subsequent discussion will focus on the AA and AB heterostructures. AIMD simulations are conducted to further assess the stability of the AA and AB heterostructures, as illustrated in Fig. 8. The total energy per atom in both heterostructures exhibits fluctuations of less than 0.05 eV, and the structures remain stable without significant deformation after heating, which provides further evidence of their structural stability.

The mechanical properties of DB-SiH/DB-SiF heterostructures are also discussed in Table 3. For the case of AA heterostructure, the calculated elastic constants of C_{11}, C_{12} and C_{66} are 148.41, 58.40 and 45.00 N/m, respectively. For the case of AB heterostructure, the calculated elastic constants of C_{11}, C_{12} and C_{66} are 159.00, 49.26 and 54.87 N/m, respectively. For each case, $C_{66} = (C_{11}-C_{12})/2 > 0$, $C_{11} > 0$, $C_{11} > |C_{12}|$ and $C_{11}C_{22}\text{-}C_{12}^2 > 0$, which fully meet the criterion of mechanical stability of 2D materials, suggesting their good

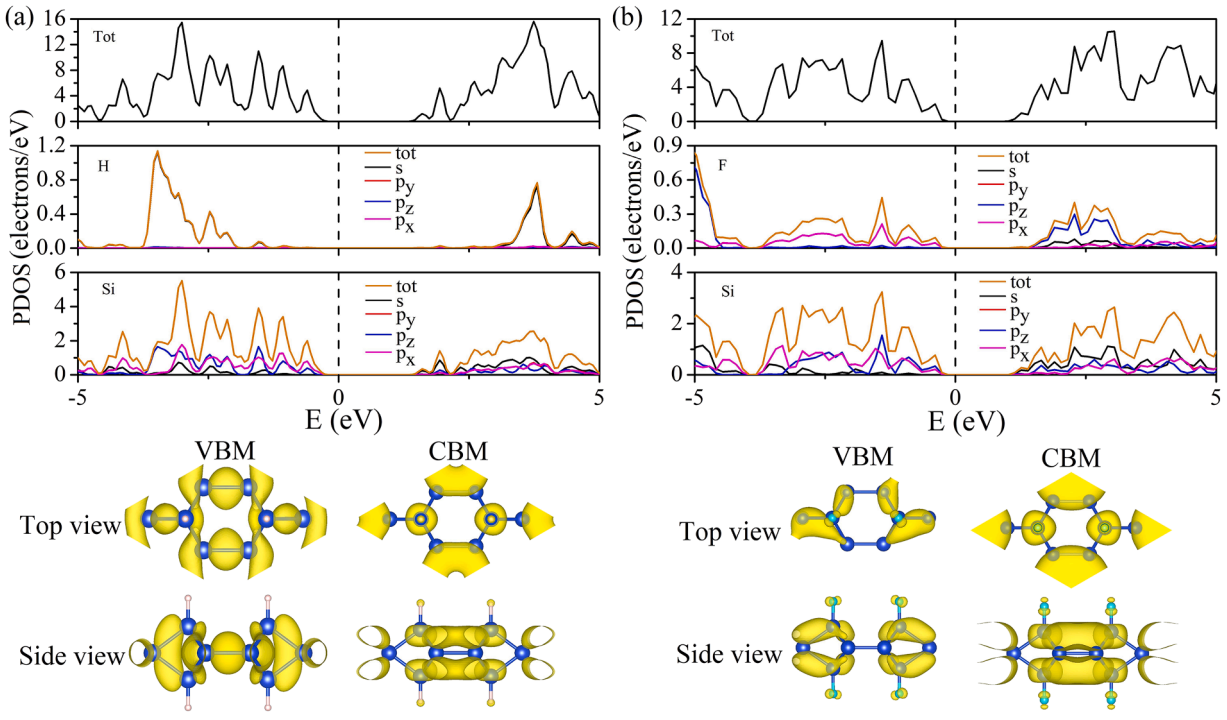

Fig. 5. Partial density of states (PDOS) and the charge density distributions of CBM and VBM for the cases of (a) DB-SiH and (b) DB-SiF. The black dotted line represents the Fermi level, which is set to 0 eV. The value of the isosurface of CBM and VBM is 0.0003 e/Å^3.

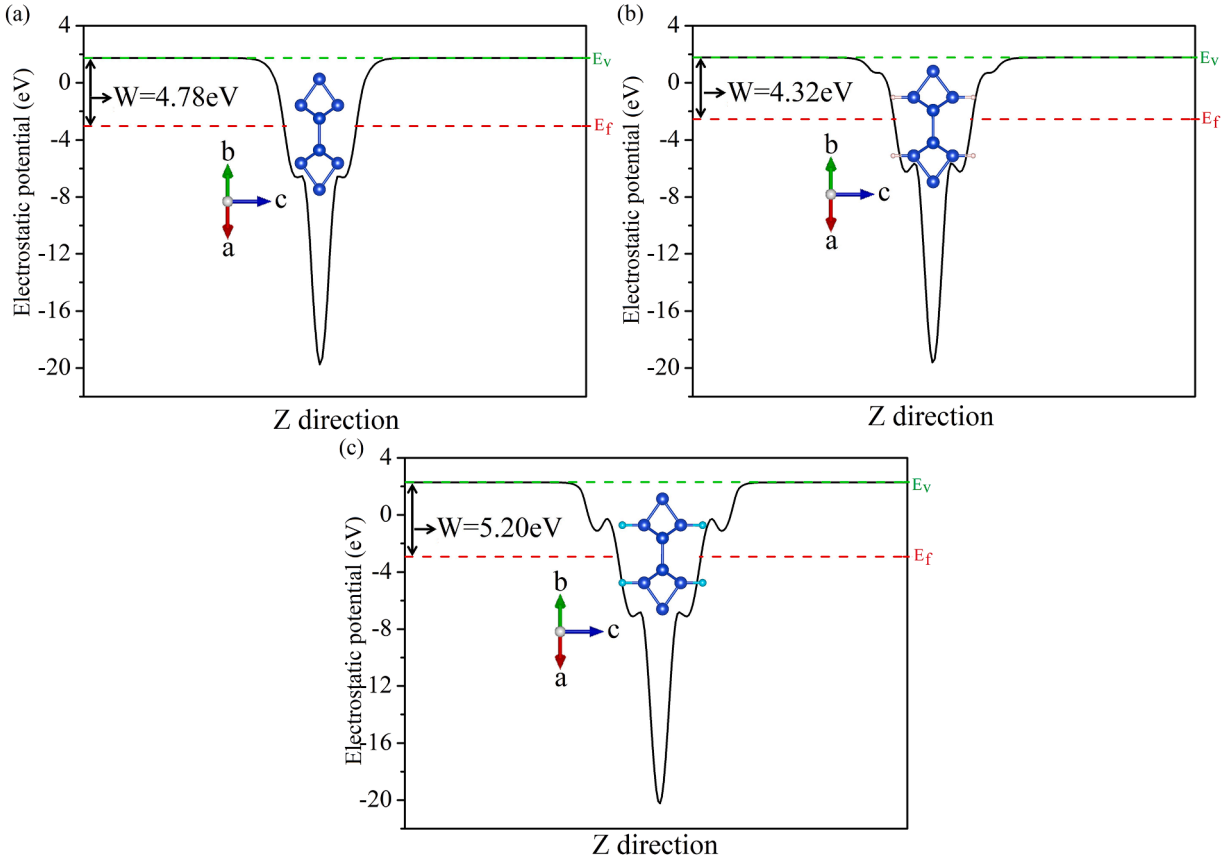

Fig. 6. The electrostatic potentials of (a) DB-Si, (b) DB-SiH and (c) DB-SiF monolayers.

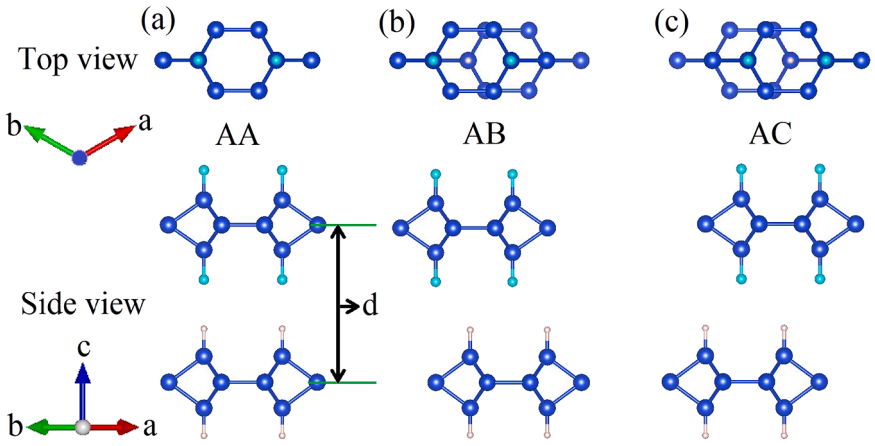

Fig. 7. The relaxed structures of the different stacking types of the DB-SiH/DB-SiF heterostructures. (a) AA stacking. (b) AB stacking. (c) AC stacking.

mechanical stability. Particularly, the values of *Y, G* and *V* for AA heterostructure are 125.43 N/m, 45.00 N/m and 0.39, respectively. As for the case of AB heterostructure, the values of *Y, G* and *V* are 143.73 N/m, 54.87 N/m and 0.31, respectively. It is noted that these parameters are much more than those of individual monolayer, suggesting their excellent rigidity and shear deformation resistance, indicating that these structures have good structural stability and low plastic deformation characteristics.

Fig. 9 shows the band structures and corresponding charge density distributions of CBM and VBM of AA and AB heterostructures. The CBM and VBM are both situated at the G point of the Brillouin zone, indicating a direct band gap of 0.52 eV for the AA heterostructure, as calculated using the HSE06 method (Fig. 9a). Similarly, the AB heterostructure exhibits a direct band gap of 0.59 eV

Table 2
Structure/electronic properties of DB-SiH/DB-SiF heterostructures with different stacking structures, including the lattice parameters (a and b), bond length (d), the interlayer distance (d), binding energy per cell (E_b), bandgaps (E_g) calculated by PBE and HSE06 methods, the work function (W) and the amount of charge transfer between DB-SiH and DB-SiF.

Systems	a=b (Å)	d_{Si-H} (Å)	d_{Si-F} (Å)	h (Å)	E_b (meV)	E_g^{PBE} (eV)	E_g^{HSE06} (eV)	Type	W (eV)	C (e)
AA	7.404	1.50	1.62	8.57	-127	0.10	0.52 (D)	II	4.76	0.0232
AB	7.404	1.50	1.62	8.54	-132	0.12	0.59 (D)	II	4.77	0.0128
AC	7.404	1.50	1.62	8.56	-112	0.12	0.59 (D)	II	4.77	0.0124

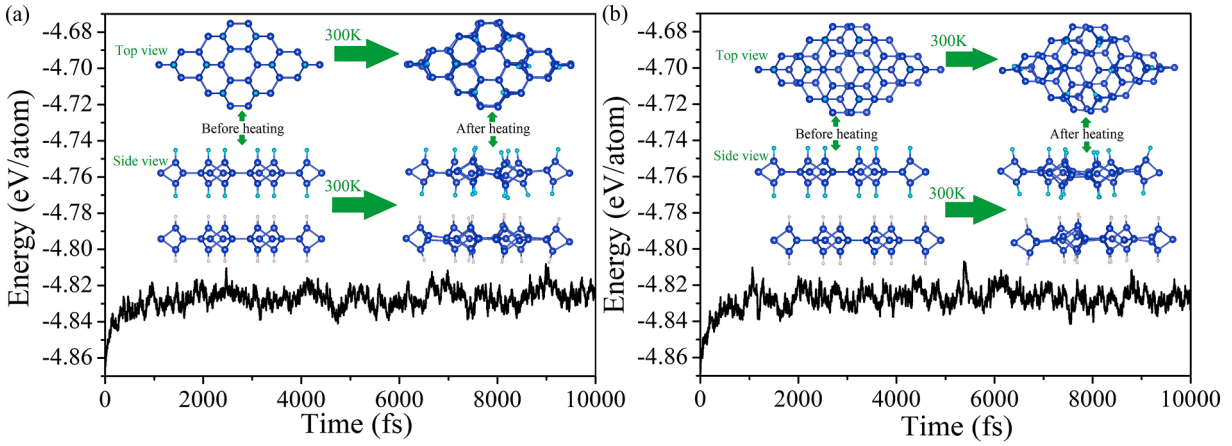

Fig. 8. The results of AIMD for DB-SiH/DB-SiF heterostructures for AA and AB stacking types. Here the supercell lattices denote the initial and final structures before and after heating.

Table 3
The elastic constants C_{ij}, the Youngs's Modulus (Y), Shear Modulus (S) and Poisson's ratio (V).

Systems	C_{11} (N/m)	C_{12} (N/m)	C_{66} (N/m)	Y (N/m)	S (N/m)	V
DB-Si	78.62	25.08	26.70	70.62	26.70	0.31
DB-SiH	78.77	22.77	28.00	72.18	28.00	0.29
DB-SiF	80.70	26.18	27.26	72.20	27.26	0.32
AA	148.41	58.40	45.00	125.43	45.00	0.39
AB	159.00	49.26	54.87	143.73	54.87	0.31

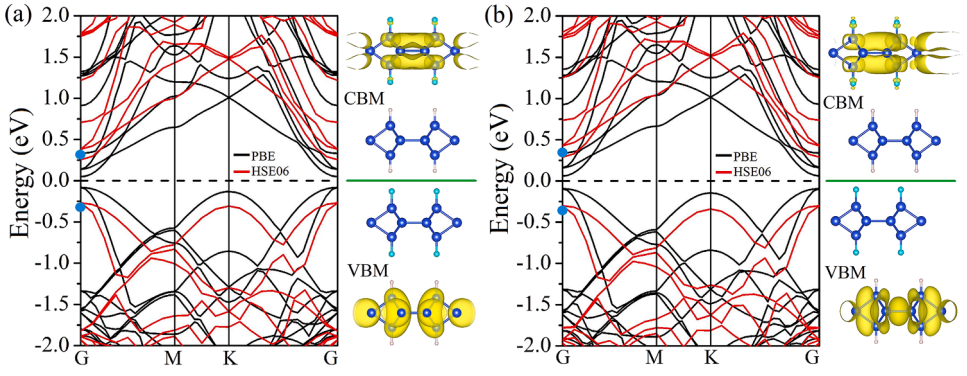

Fig. 9. (a)-(b) The band structures and corresponding charge density distributions of CBM and VBM for AA and AB DB-SiH/DB-SiF heterostructures. The Fermi level is at 0 eV. The value of the isosurface of CBM and VBM is 4×10^{-8} e/Å^3.

(Fig. 9b). In comparison to the band gaps of the DB-SiH and DB-SiF monolayers, the heterostructures display a significantly smaller band gap, which may be attributed to the weak interlayer interaction between H and F atoms. The charge density distributions of the CBM are predominantly derived from the monolayer DB-SiF, with a significant contribution from Si-Si bonds and a minor contribution from F atoms. Conversely, the charge density distributions are derived exclusively from Si-Si bonds in the monolayer DB-SiH, which indicates the influence of interlayer interaction between H and F atoms on the band structure. The aforementioned discussions illustrate that the charge density distributions of the CBM and VBM are entirely distinct, exhibiting a pronounced type-II band arrangement. This implies a substantial separation of electrons and holes in AA and AB heterostructures. It is widely acknowledged that the effective separation of electrons and holes is crucial for enhancing the photocatalytic activity of 2D materials. Consequently, these heterostructures will be highly beneficial in the field of photocatalysis.

To better understand the band structures of the heterostructures, the band edge positions of DB-SiH monolayer, DB-SiF monolayer, AA heterostructure, and AB heterostructure are discussed. As shown in Fig. 10, the band edge arrangement with respect to the vacuum energy level before and after the heterostructure formed is presented. It is observed that the Fermi level of the DB-SiF monolayer is situated at a lower energy level than that of the DB-SiH monolayer. When DB-SiF is stacked on DB-SiH, an electron transfer occurs from DB-SiH to DB-SiF, while a hole transfer occurs from DB-SiF to DB-SiH. It is also noteworthy that the Fermi levels of the two DB-SiH/DB-SiF heterostructures are consistently situated between the Fermi levels of their respective monolayers. This phenomenon may be attributed to the potential alteration at the interface resulting from the redistribution of charge. Additionally, for each heterostructure, it is observed that the band edge positions of the DB-SiH and DB-SiF are cross-distributed, which further substantiates its type-II band alignment characteristics.

Next, we study the work function by calculating the electrostatic potentials of DB-SiH/DB-SiF heterostructures. Due to the asymmetry of the upper and lower surfaces of the heterostructure, the dipole correction [52] is also considered in the calculations. As shown in Fig. 11 (a)-(b), The work function values of AA and AB heterostructures are 4.76 eV and 4.77 eV, respectively, which fall between the work function of monolayer DB-SiH (4.32 eV) and monolayer DB-SiF (5.20 eV). This indicates that a substantial charge transfer occurs between DB-SiH and DB-SiF. In order to verify this point, the corresponding CDD and the Bader charge analysis are discussed in detail. In the case of the AA heterostructure, approximately 0.0232 electrons can be transferred from the monolayer DB-SiH to the monolayer DB-SiF, while for the AB heterostructure, approximately 0.0128 electrons can be transferred from the monolayer DB-SiH to the monolayer DB-SiF. Consequently, an electron redistribution occurs at the interface, indicating the presence of a significant build-in field between monolayer DB-SiH and monolayer DB-SiF. This phenomenon has been observed in other vertical heterostructures, including Janus-In_2STe/InSe [53], SiC/InSe [54], and DLHS-AlAs/germanene [55] vdW heterostructures.

As discussed above, these DB-SiH/DB-SiF heterostructures are direct band gap semiconductors with a type-II band arrangement, rendering them appropriate for utilisation in a multitude of optoelectronic devices. A further investigation of their optical properties will therefore be conducted. The optical absorption coefficient, reflectivity, and energy loss spectrum of DB-Si, DB-SiH, DB-SiF, and DB-SiH/DB-SiF heterostructures for AA and AB stacking types are illustrated in Fig. 12. Since the heterostructure is vertically stacked, the focus of our discussion is the optical properties perpendicular to the two-dimensional plane. The corresponding optical parameters are calculated using the following formulas:

$$\alpha(\omega) = \sqrt{2}\omega\left[\sqrt{\varepsilon_1{}^2(\omega) + \varepsilon_2{}^2(\omega)} - \varepsilon_1(\omega)\right]^{1/2} \tag{9}$$

$$R(\omega) = \left|\frac{\sqrt{\varepsilon_1(\omega) + i\varepsilon_2(\omega)} - 1}{\sqrt{\varepsilon_1(\omega) + i\varepsilon_2(\omega)} + 1}\right|^2 \tag{10}$$

$$L(\omega) = \frac{\varepsilon_2(\omega)}{\varepsilon_1{}^2(\omega) + \varepsilon_2{}^2(\omega)} \tag{11}$$

where optical absorption coefficient, reflectivity function, energy loss function, the real part and imaginary part of the complex dielectric function are indicated by $\alpha(\omega)$, $R(\omega)$, $L(\omega)$, $\varepsilon_1(\omega)$ and $\varepsilon_2(\omega)$, respectively.

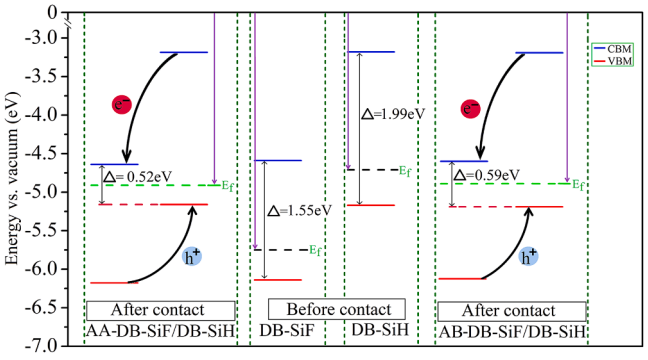

Fig. 10. Band alignment before and after DB-SiH/DB-SiF heterostructures contact. The vacuum energy level is set to 0 eV.

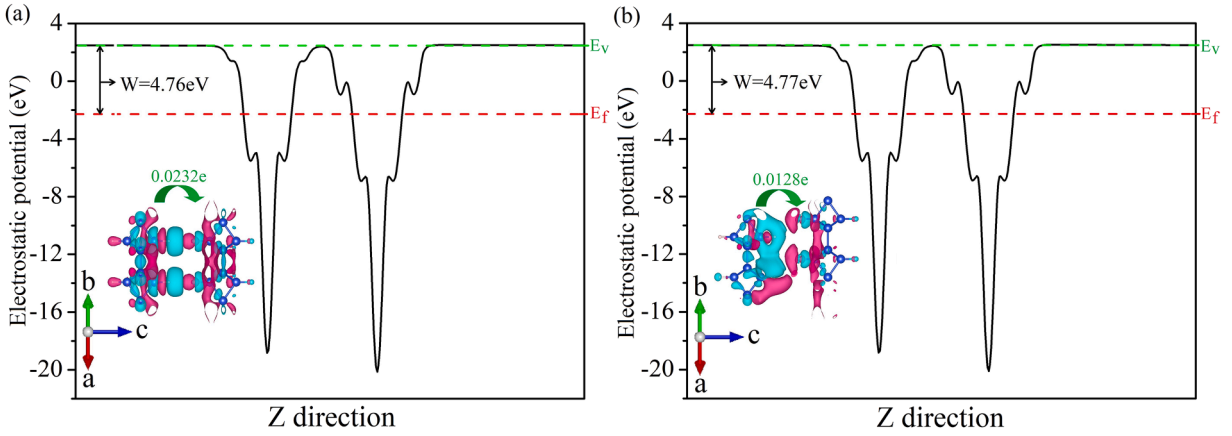

Fig. 11. The electrostatic potentials of DB-SiH/DB-SiF heterostructures for (a) AA and (b) AB stacking types. Here, the charge density difference (CDD) of the heterostructures are also presented.

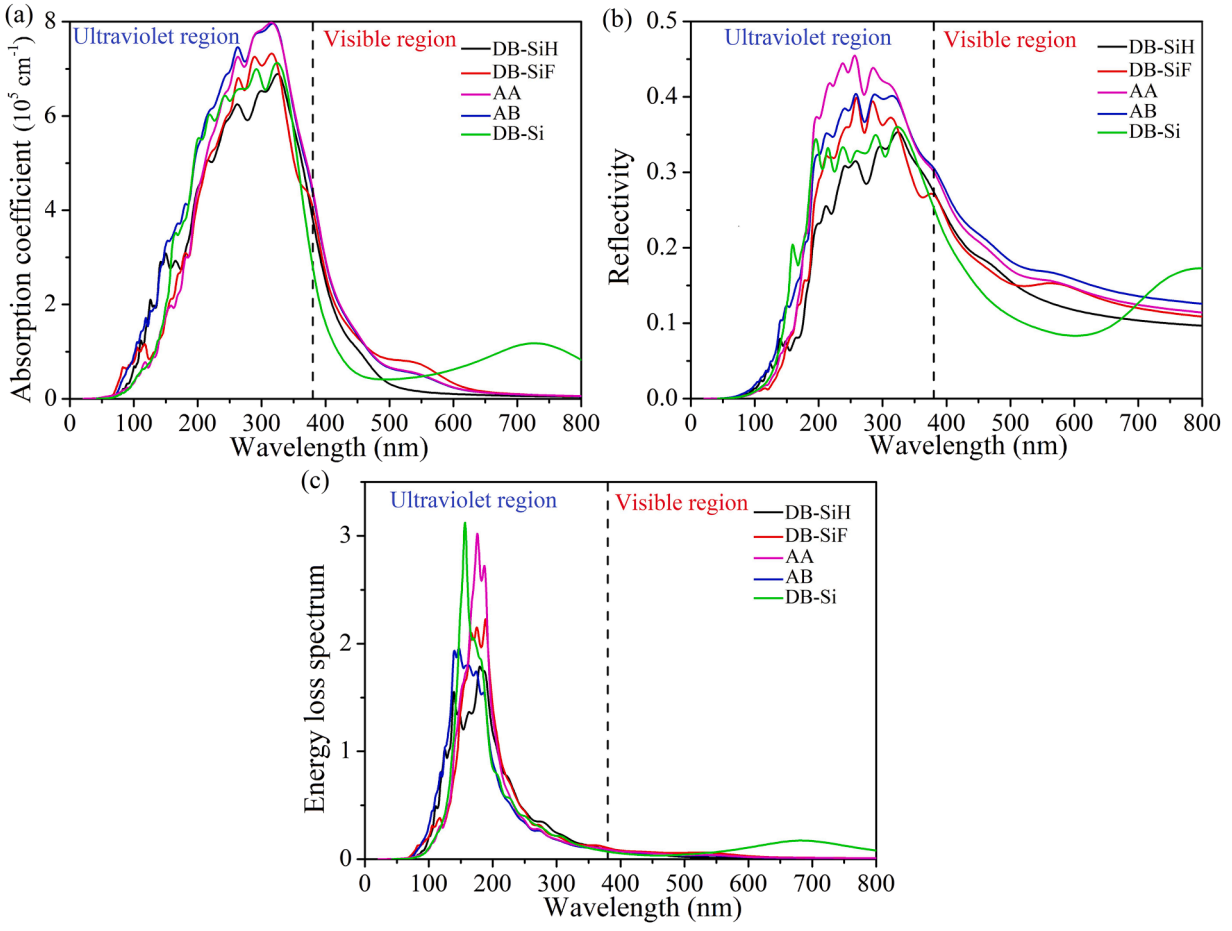

Fig. 12. (a) The optical absorption coefficient, (b) reflectivity and (c) energy loss spectrum of DB-Si, DB-SiH, DB-SiF, DB-SiH/DB-SiF heterostructures for AA and AB stacking types.

As shown in Fig. 12 (a), all the cases have relatively high absorption coefficients with values exceeding 7×10^5 cm^{-1} in the ultraviolet region. Especially, the maximum absorption coefficient of heterostructures can reach up to 8×10^5 cm^{-1}. In the visible light region, the maximum optical absorption coefficient of the pristine DB-Silicene can reach up to 3×10^5 cm^{-1}. After hydrogenation and fluorination, the absorption coefficient of visible light can be enhanced. Specifically, the maximum visible light absorption coefficients

of DB-SiH and DB-SiF monolayers are close to 4×10^5 cm^{-1}. Besides, the maximum visible light absorption coefficients of two DB-SiH/DB-SiF heterostructures are larger than those of the individual monolayers. Therefore, it can be concluded that the chemical functionalization and construction of heterostructures can improve light absorption from ultraviolet to visible light, indicating that these new structures have valuable applications in optoelectronics.

The reflectivity $R(\omega)$ measures the ability of solid materials to reflect photon energy. As illustrated in Fig. 12(b), the maximum reflectivity coefficient of pristine DB-Silicene in the ultraviolet region is approximately 0.35. In contrast, the reflectivity coefficients of two DB-SiH/DB-SiF heterostructures are enhanced, with the maximum reflectivity of the AA heterostructure reaching 0.45 in the 200–300 nm range. Similarly, in the visible light range of 380–680 nm, the maximum reflectivity coefficient of pristine DB-Silicene decreases to 0.25, which is lower than that of all other systems. In particular, the reflectivity coefficients of the two functionalised DB-Silicene monolayers exceed that of the pristine DB-Silicene, while the coefficients of the two heterostructures surpass those of the functionalised DB-Silicene monolayers. Overall, the findings suggest that functionalised DB-Silicene monolayers and their heterostructures display enhanced sensitivity to ultraviolet and visible light reflection.

The electron energy loss function $L(\omega)$ refers to the energy loss of photoelectrons as they propagate through a uniform dielectric. As shown in Fig. 12 (c), the energy loss functions in the ultraviolet region exhibit more pronounced changes compared to the visible region. The maximum peak values of the DB-SiH monolayer and AB heterostructure are even less than 2.0. The DB-SiF monolayer and AA heterostructure have maximum peak values of 2.2 and 3.0, respectively, which are lower than that of pristine DB-Silicene. Additionally, these two structures show a clear trend of red shift in comparison to the pristine DB-Silicene monolayer.

4. Conclusion

In summary, the structural, mechanical and optoelectronic properties of hydrogenated and fluorinated dumbbell silicene monolayers and their heterostructures are systematically investigated by first-principles calculations. The results demonstrate that the hydrogenated and fluorinated dumbbell silicene monolayers as well as heterostructures exhibit excellent structural, energetic, thermal and mechanical stability. The DB-SiH and DB-SiF monolayers have been observed to exhibit direct band gap characteristics with a value of 1.99 eV and an indirect band gap of 1.55 eV, respectively. The work function of the DB-SiH monolayer is observed to be lower than that of pristine DB-Silicene, whereas the work function of the DB-SiF monolayer is found to be higher than that of pristine DB-Silicene. Moreover, the DB-SiH/DB-SiF heterostructures display a narrow direct band gap with values of 0.52 eV (AA stacking) and 0.59 eV (AB stacking), respectively, and indicate a typical type-II band arrangement. The significant charge transfer from DB-SiH to DB-SiF induces the formation of a built-in electric field at the interface of the heterostructures, which facilitates the effective separation of electrons and holes. Meanwhile, the maximum visible light absorption coefficients of the DB-SiH and DB-SiF monolayers are approximately 4×10^5 cm^{-1}. The maximum visible light absorption coefficients of two DB-SiH/DB-SiF heterostructures are larger than those of the individual monolayers. Additionally, these modified structures exhibit enhanced sensitivity to the reflection of ultraviolet and visible light. These significant findings collectively suggest that these new structures have valuable applications in optoelectronic devices.

CRediT authorship contribution statement

Gang Guo: Writing – review & editing, Writing – original draft, Visualization, Validation, Supervision, Software, Methodology, Investigation, Funding acquisition, Formal analysis, Data curation. **Fuming Du:** Visualization, Investigation, Funding acquisition, Formal analysis, Data curation. **Gencai Guo:** Visualization, Software, Methodology, Investigation. **Ping Li:** Writing – review & editing, Visualization, Supervision, Software, Methodology, Investigation, Formal analysis.

Declaration of interests

The authors declare that they have no known competing financial interests or personal relationships that could have appeared to influence the work reported in this paper.

Acknowledgements

This work is supported by the Scientific Research Fund of Hunan Provincial Education Department (24B0847, 23A0630), by the Micro and Nano optoelectronic Devices and Integrated Technology Key Laboratory of Hunan Institute of Technology, numbered KFA24037, by the Natural Science Foundation of Hunan Province (2023JJ50101), by the College Students' Innovation and Entrepreneurship Training Program of Hunan Province (S202411528135, S202411528098).

References

[1] K.S. Novoselov, A.K. Geim, S.V. Morozov, D. Jiang, Y. Zhang, S.V. Dubonos, I.V. Grigorieva, A.A. Firsov, Science 306 (2004) 666–669, https://doi.org/10.1126/science.1102896.

[2] L.A. Chernozatonskii, A.A. Artyukh, A.G. Kvashnin, Mechanical engineering effect in electronic and optical properties of graphene nanomeshes, ACS Appl. Mater. Interf. 12 (49) (2020) 55189–55194, https://doi.org/10.1021/acsami.0c17060.

[3] G.G. Naumis, S. Barraza-Lopez, M. Oliva-Leyva, H. Terrones, Electronic and optical properties of strained graphene and other strained 2D materials: a review, Rep. Prog. Phys. 80 (9) (2017) 096501, https://doi.org/10.1088/1361-6633/aa74ef.

[4] P. Vogt, P.D. Padova, C. Quaresima, J. Avila, E. Frantzeskakis, M.C. Asensio, A. Resta, B. Ealet, G.L. Lay, Silicene: compelling experimental evidence for, graphene like two-dimensional silicon, Phys. Rev. Lett. 108 (2012) 155501, https://doi.org/10.1103/PhysRevLett.108.155501.

[5] S. Chae, T.H. Le, C.S. Park, Y. Choi, S. Kim, U. Lee, E. Heo, H. Lee, Y.A. Kim, O.S. Kwo, H. Yoon, Anomalous restoration of sp^2 hybridization in graphene functionalization, Nanoscale 12 (25) (2020) 13351–13359, https://doi.org/10.1039/D0NR03422C.

[6] E. Cinquanta, E. Scalise, D. Chiappe, C. Grazianetti, B.V.D. Broek, M. Houssa, M. Fanciulli, A. Molle, Getting through the nature of silicene: an sp^2-sp^3 two-dimensional silicon nanosheet, J. Phys. Chem. C 117 (32) (2013) 16719–16724, https://doi.org/10.1021/jp405642g.

[7] Z.G. Shao, X.S. Ye, L. Yang, C.L. Wang, First-principles calculation of intrinsic carrier mobility of silicene, J. Appl. Phys. 114 (9) (2013) 093712, https://doi.org/10.1063/1.4820526.

[8] S. Rachel, M. Ezawa, Giant magnetoresistance and perfect spin filter in silicene, germanene, and stanene, Phys. Rev. B 89 (19) (2014) 195303, https://doi.org/10.1103/PhysRevB.89.195303.

[9] R.E. Roman, S.W. Cranford, Mechanical properties of silicene, Comput. Mater. Sci. 82 (2014) 50–55, https://doi.org/10.1016/j.commatsci.2013.09.030.

[10] S. Sahoo, A. Sinha, N.A. Koshi, S.C. Lee, S. Bhattacharjee, B. Muralidharan, Silicene: an excellent material for flexible electronics, J. Phys. D: Appl. Phys. 55 (42) (2022) 425301, https://doi.org/10.1088/1361-6463/ac8080.

[11] C.C. Liu, H. Jiang, Y. Yao, Low-energy effective Hamiltonian involving spin-orbit coupling in silicene and two-dimensional germanium and tin, Phys. Rev. B 84 (19) (2011) 195430, https://doi.org/10.1103/PhysRevB.84.195430.

[12] C.L. Lin, R. Arafune, K. Kawahara, N. Tsukahara, E. Minamitani, Y. Kim, N. Takagi, M. Kawai, Structure of silicene grown on Ag (111), Appl. Phys. Express 5 (4) (2012) 045802, https://doi.org/10.1143/APEX.5.045802.

[13] T. Jaroch, R. Zdyb, Temperature-dependent growth and evolution of silicene on Au ultrathin films-LEEM and LEED studies, Materials 15 (4) (2022) 1610, https://doi.org/10.3390/ma15041610.

[14] T. Morishita, M.J.S. Spencer, S. Kawamoto, L.K. Snook, A new surface and structure for silicene: polygonal silicene formation on the Al (111) surface, J. Phys. Chem. C 117 (42) (2013) 22142–22148. https://pubs.acs.org/doi/abs/10.1021/jp4080898.

[15] F. Matusalem, M. Marques, L.K. Teles, F. Bechstedt, Stability and electronic structure of two-dimensional allotropes of group-IV materials, Phys. Rev. B 92 (2015) 045436, https://doi.org/10.1103/PhysRevB.92.045436.

[16] L. Shu, Y.J. Xia, B. Li, L. Peng, H.Z. Shao, Z.G. Wang, Y. Cen, H.Y. Zhu, H. Zhang, Full-landscape selection rules of electrons and phonons and temperature-induced effects in 2D silicon and germanium allotropes, NPJ Comput. Mater. 10 (1) (2024) 2, https://doi.org/10.1038/s41524-023-01162-w.

[17] B. Peng, H. Zhang, H.Z. Shao, Y.F. Xu, R.J. Zhang, H.L. Lu, D.W. Zhang, H.Y. Zhu, First-principles prediction of ultralow lattice thermal conductivity of dumbbell silicene: a comparison with low-buckled silicene, ACS Appl. Mater. Interf. 8 (32) (2016) 20977–20985, https://doi.org/10.1021/acsami.6b04211.

[18] D. Kaltsas, L. Tsetseris, Stability and electronic properties of ultrathin films of silicon and germanium, Phys. Chem. Chem. Phys. 15 (2013) 9710–9715, https://doi.org/10.1039/C3CP50944C.

[19] S. Cahangirov, V.O. Özçelik, A. Rubio, S. Ciraci, Silicite: the layered allotrope of silicon, Phys. Rev. B 90 (2014) 085426, https://doi.org/10.1103/PhysRevB.90.085426.

[20] V.O. Özçelik, D. Kecik, E. Durgun, S. Ciraci, Adsorption of group IV elements on graphene, silicene, germanene, and stanene: dumbbell formation, J. Phys. Chem. C 119 (2015) 845–853, https://doi.org/10.1021/jp5106554.

[21] Y. Han, J.M. Dong, G.Z. Qin, M. Hu, Phonon transport in the ground state of two-dimensional silicon and germanium, RSC Adv. 6 (74) (2016) 69956–69965, https://doi.org/10.1039/C6RA14351B.

[22] G. Guo, S.Y. Tan, G.C. Guo, Z.X. Xie, Strain-enhanced properties of Janus Si_2PAs monolayer as a promising photocatalyst for the splitting of water: insights from first-principles calculations, Coll. Surf. A: Physicochem. Eng. Asp. 659 (2023) 130782, https://doi.org/10.1016/j.colsurfa.2022.130782.

[23] C.M. Ke, Y.P. Wu, G.Y. Guo, W. Lin, Z.M. Wu, C.J. Zhou, J.Y. Kang, Tuning the electronic, optical, and magnetic properties of monolayer GaSe with a vertical electric field, Phys. Rev. Appl. 9 (4) (2018) 044029, https://doi.org/10.1103/PhysRevApplied.9.044029.

[24] H. Zhu, X. Gan, A. McCreary, R. Lv, Z. Lin, M. Terrones, Heteroatom doping of two-dimensional materials: from graphene to chalcogenides, Nano Today 30 (2020) 100829, https://doi.org/10.1016/j.nantod.2019.100829.

[25] L.M. Yang, K. Majumdar, H. Liu, Y.C. Du, H. Wu, M. Hatzistergos, P.Y. Hung, R. Tieckelmann, W. Tsai, C. Hobbs, P.D. Ye, Chloride molecular doping technique on 2D materials: WS_2 and MoS_2, Nano Lett. 14 (11) (2014) 6275–6280, https://doi.org/10.1021/nl502603d.

[26] L.M. Yang, K. Majumdar, H. Liu, Y.C. Du, H. Wu, M. Hatzistergos, P.Y. Hung, R. Tieckelmann, W. Tsai, C. Hobbs, P.D. Ye, Surface functionalization for magnetic property tuning of nonmagnetic 2D materials, Adv. Mater. Interf. 9 (3) (2022) 2100463, https://doi.org/10.1002/admi.202100463.

[27] J.H. Jeong, S. Kang, N. Kim, R. Joshi, G.H. Lee, Recent trends in covalent functionalization of 2D materials, Phys. Chem. Chem. Phys. 24 (18) (2022) 10684, https://doi.org/10.1039/d1cp04831g, 10684-10711.

[28] X. Zhao, F. Liu, J. Ren, F.Y. Qu, Valleytronic and magneto-optical properties of Janus and conventional $TiBrI/CrI_3$ and TiX_2/CrI_3 (X= Br, I) heterostructures, Phys. Rev. B 104 (8) (2021) 085119, https://doi.org/10.1103/PhysRevB.104.085119.

[29] R.J. Sun, J.J. Lu, X.W. Zhao, G.C. Hu, X.B. Yuan, J.F. Ren, Robust valley polarization induced by super-exchange effects in HfNX(X=Cl, Br, I)/$FeCl_2$ two-dimensional ferrovalley heterostructures, Appl. Phys. Lett. 120 (2022) 063103, https://doi.org/10.1063/5.0080466.

[30] R.J. Sun, R. Liu, J.J. Lu, X.W. Zhao, G.C. Hu, X.B. Yuan, J.F. Ren, Reversible switching of anomalous valley Hall effect in ferrovalley Janus 1T-CrOX (X= F, Cl, Br, I) and the multiferroic heterostructure CrOX/In_2Se_3, Phys. Rev. B 105 (23) (2022) 235416, https://doi.org/10.1103/PhysRevB.105.235416.

[31] J. Zhao, H. Zeng, Chemical functionalization of pentagermanene leads to stabilization and tunable electronic properties by external tensile strain, ACS Omega 2 (1) (2017) 171–180, https://doi.org/10.1021/acsomega.6b00439.

[32] D.M. Hoat, V.V. On, D.K. Nguyen, M. Naseri, R. Ponce-Pérez, T.V. Vu, J.F. RivasSilva, N.N. Hieu, G.H. Cocoletzi, Structural, electronic and optical properties of pristine and functionalized MgO monolayers: a first principles study, RSC Adv. 10 (66) (2020) 4041–40420, https://doi.org/10.1039/D0RA05030J.

[33] D.M. Hoat, D.K. Nguyen, V.V. On, J.F. RivasSilva, G.H. Cocoletzi, Opening the germanene monolayer band gap using halogen atoms: an efficient approach studied by first-principles calculations, Appl. Surf. Sci. 551 (2021) 149318, https://doi.org/10.1016/j.apsusc.2021.149318.

[34] A. Bao, X. Li, X. Guo, H.T. Yao, M.G. Chen, Tuning the structural, electronic, mechanical and optical properties of silicene monolayer by chemical functionalization: a first-principles study, Vacuum 203 (2022) 111226, https://doi.org/10.1016/j.vacuum.2022.111226.

[35] G. Guo, Y. Xu, G. Guo, Janus-functionalization induced magnetism and improved optoelectronic properties in two-dimension silicene and germanene: insights from first-principles calculations, J. Phys.: Condens. Matter 35 (33) (2023) 335501, https://doi.org/10.1088/1361-648X/acd50d.

[36] G. Guo, J. Liu, Y. Xu, G.C. Guo, S.Y. Tan, Chemical functionalization induced photocatalytic performance for water splitting of silicene: a first-principles investigation, Coll. Surf. A: Physicochem. Eng. Asp. 667 (2023) 131379, https://doi.org/10.1016/j.colsurfa.2023.131379.

[37] F. Karlický, K.K.R. Datta, M. Otyepka, R. Zbořil, Halogenated graphenes: rapidly growing family of graphene derivatives, ACS Nano 7 (8) (2013) 6434–6464, https://doi.org/10.1021/nn4024027.

[38] J.L. Qiu, H.X. Fu, Y. Xu, Q. Zhou, S. Meng, H. Li, L. Chen, K.H. Wu, From silicene to half-silicane by hydrogenation, ACS Nano 9 (11) (2015) 11192–11199, https://doi.org/10.1021/acsnano.5b04722.

[39] G. Kresse, J. Furthmüller, Efficient iterative schemes for ab initio total-energy calculations using a plane-wave basis set, Phys. Rev. B 54 (1996) 11169, https://doi.org/10.1103/PhysRevB.54.11169.

[40] G. Kresse, J. Joubert, From ultrasoft pseudopotentials to the projector augmented wave method, Phys. Rev. B 59 (1999) 1758–1775, https://doi.org/10.1103/PhysRevB.59.1758.

[41] J.P. Perdew, K. Burke, M. Ernzerhof, Generalized gradient approximation made simple, Phys. Rev. Lett. 77 (18) (1996) 3865, https://doi.org/10.1103/PhysRevLett.77.3865.

[42] B. Hammer, L.B. Hansen, J.K. Nørskov, Improved adsorption energetics within density-functional theory using revised Perdew-Burke-Ernzerhof functionals, Phys. Rev. B 59 (11) (1999) 7413, https://doi.org/10.1103/PhysRevB.59.7413.

[43] J. Heyd, G.E. Scuseria, M. Ernzerhof, Hybrid functionals based on a screened Coulomb potential, J. Chem. Phys. 118 (2003) 8207–8215, https://doi.org/10.1063/1.1564060.

[44] M. Marsman, J. Paier, A. Stroppa, Hybrid functionals applied to extended systems, J. Phys. Condens. Matter 20 (2008) 064201, https://doi.org/10.1088/0953-8984/20/6/064201.
[45] G. Guo, Y. Zhou, G.C. Guo, Z.X. Xie, First-principles study on the optoelectronic and photocatalytic properties of the C_{2h}-Janus Al_2XY (X/Y=S, Se and Te) monolayers, Mater. Today Chem. 35 (2024) 101913, https://doi.org/10.1016/j.mtchem.2024.101913.
[46] Q. Yang, S.L. Zhang, X.P. Chen, M. Cai, C.J. Tan, Fluorosilicene/chlorosilicene bilayer semiconductor with tunable electronic and optical properties, J. Appl. Phys. 121 (5) (2017) 055701, https://doi.org/10.1063/1.4975194.
[47] G. Guo, L. Mao, K. Liu, X.C. Tan, Pd-Adsorbed SiN_3 monolayer as a promising gas scavenger for SF_6 partial discharge decomposition components: insights from the first-principles study, Langmuir 40 (14) (2024) 7669–7679, https://doi.org/10.1021/acs.langmuir.4c00370.
[48] E. Cadelano, P.L. Palla, S. Giordano, L. Colombo, Elastic properties of hydrogenated graphene, Phys. Rev. B 82 (23) (2010) 235414, https://doi.org/10.1103/PhysRevB.82.235414.
[49] R.C. Andrew, R.E. Mapasha, A.M. Ukpong, N. Chetty, Mechanical properties of graphene and boronitrene, Phys. Rev. B 85 (12) (2012) 125428, https://doi.org/10.1103/PhysRevB.85.125428.
[50] Q. Yue, J. Kang, Z. Shao, X. Zhang, S. Chang, G. Wang, S. Qin, J. Li, Mechanical and electronic properties of monolayer MoS_2 under elastic strain, Phys. Lett. A 376 (2012) 1166–1170, https://doi.org/10.1016/j.physleta.2012.02.029.
[51] Q. Yang, C.J. Tan, R.S. Meng, J.K. Jiang, Q.H. liang, X. Sun, D.G. Yang, X.P. Chen, The intriguing electronic and optical properties modulation of hydrogen and fluorine codecorated silicene layers, Appl. Surf. Sci. 398 (2017) 73–80, https://doi.org/10.1016/j.apsusc.2016.11.226.
[52] L. Bengtsson, Dipole correction for surface supercell calculations, Phys. Rev. B 59 (19) (1999) 12301, https://doi.org/10.1103/PhysRevB.59.12301.
[53] X.P. Li, B.X. Zhai, X.H. Song, Y. Yan, J.B. Li, C.X. Xia, Two-dimensional Janus-In_2STe/InSe heterostructure with direct gap and staggered band alignment, Appl. Surf. Sci. 509 (2020) 145317, https://doi.org/10.1016/j.apsusc.2020.145317.
[54] Z. Wang, Y. Zhang, X. Wei, T.T. Guo, J.B. Fan, L. Ni, Y.J. Weng, Z.D. Zha, J. Liu, Y. Tian, T. Lia, L. Duan, Type-II tunable SiC/InSe heterostructures under an electric field and biaxial strain, Phys. Chem. Chem. Phys. 22 (17) (2020) 9647–9655, https://doi.org/10.1039/D0CP00291G.
[55] G. Guo, Y.C. Chen, L.Y. Mao, P. Li, Stacking order and vertical strain controllable optoelectronic properties of van der Waals heterostructures constructed with germanene and double layer hexagonal structure AlAs, Surf. Interf. 55 (2024) 105413, https://doi.org/10.1016/j.surfin.2024.105413.